

A Study on the FPGA Implementation of the Bilateral Control Algorithm Towards Haptic Teleoperation

DOI 10.7305/automatika.54-1.302
UDK 681.51.07-519:612.88; 004.896
IFAC 4.0.6; 1.2.1

Original scientific paper

This paper presents the FPGA implementation of sliding mode control algorithm for bilateral teleoperation, such that, the problem of haptic teleoperation is addressed. The presented study improves haptic fidelity by widening the control bandwidth. For wide control bandwidth, short control periods as well as short sampling periods are required that was achieved by the FPGA. The presented FPGA design methodology applies basic optimization methods in order to meet the required control period as well as the required hardware resource consumption. The circuit specification was performed by the high-level programming language LabVIEW using the fixed-point data type. Hence, short design times for producing the FPGA logic circuit can be achieved. The proposed FPGA-based bilateral teleoperation was validated by master-slave experimental device.

Key words: Bilateral teleoperation, Haptics, FPGA, Sliding Mode Control

Analiza FPGA implementacije bilateralnih algoritama upravljanja za dodirnu teleoperaciju. Ovaj rad opisuje FPGA implementaciju algoritama upravljanja kliznim režimima za bilateralnu teleoperaciju, pri čemu je opisan problem haptičke teleoperacije. Prikazano istraživanje poboljšava dodirnu pouzdanost proširenjem upravljačkog propusnog pojasa. Za široki propusni pojas, potrebni su kratki upravljački periodi i brzo vrijeme uzorkovanja, što je postignuto primjenom FPGA sklopovlja. Prikazana metodologija za projektiranje FPGA sklopovlja koristi osnovne optimizacijske metode s ciljem postizanja potrebnih upravljačkih perioda i zahtjevane fizičke iskorištenosti sklopovlja. Specifikacije sklopovlja su provedene programskim jezikom visoke razine LabVIEW uz korištenje podataka s nepomičnim decimalnim zarezom. Stoga je moguće implementirati traženu logiku na FPGA sklopovlje u kratkom vremenu. Opisana bilateralna teleoperacija temeljena na FPGA sklopovlju je testirana na eksperimentalnom postavu s nadređenim i podređenim čvorom.

Ključne riječi: bilateralna teleoperacija, haptika, FPGA, upravljanje kliznim režimima

1 INTRODUCTION

Robotic teleoperation denotes the control of remotely located robot device by a human operator. Hence, it is not required for a human operator to be physically present at the remote side. Thus, he or she can perform tasks at the inaccessible remote environment (e.g. aerospace, military, and medicine applications).

During the robotic teleoperation, the human operator generates the desired motion by the local master device for the remote robot slave device. When he or she generates the desired motion based only on visual and auditory information, then such teleoperation is called unilateral teleoperation. The latter suffers from rather difficult remote task manipulation and may additionally require long training period for the human operator. This can be improved, if the remote environment reaction force is provided to the

human operator and then such teleoperation is called bilateral teleoperation. It can be noted, that the master device is a robot device that provides reaction force to the human operator. The concept of the bilateral teleoperation is depicted by Figure 1.

Transparency optimized bilateral teleoperator could give the human operator the feeling as if he or she is physically present at the remote side. Thus, the advanced tasks, such as minimal invasive surgery (MIS), could be performed better [1], [2]. When the motion and forces are tracked simultaneously then such teleoperation is called haptic teleoperation; hence, the touch of the slave device with the remote environment is ideally transmitted to the human operator.

A few basic teleoperator architectures, such as 2-channell and 4-channell, are well-known [3]. Despite this, a lot of researchers are aimed at improving the bilateral

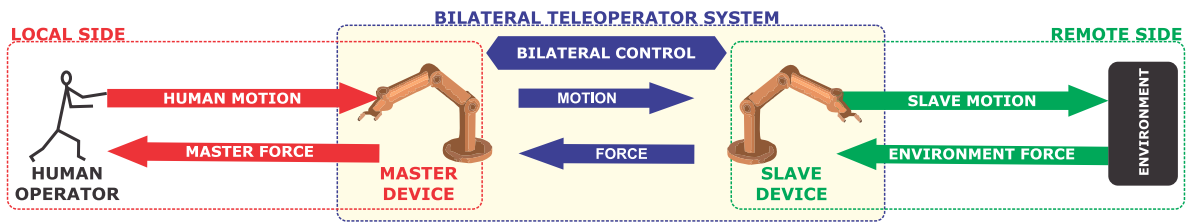


Fig. 1. Bilateral teleoperation.

teleoperation [4], [5]. Tanaka et al. obtained multi-DoF bilateral teleoperation by acceleration control [6]. Alternatively, the sliding mode control (SMC) theory provides a strong theoretical background and can also be applied to derive a robust control algorithm for linear and nonlinear systems [7]. Khan et al. obtained bilateral teleoperation by using SMC formulation [8]. However, the control of the master-slave bilateral teleoperation system may still remain cumbersome. Therefore, Ohnishi proposed a modal decomposition of the physical actuator space into independent virtual modal space in order to simplify the control design [9]. The modal transformation decomposes the bilateral teleoperation into two independent virtual modes that fit the performance requirements. Hace et al. proposed bilateral control using the chattering-free SMC design in the virtual modal space [10].

The teleoperator performance is mostly determined by the achieved control bandwidth, sampling bandwidth, and also the robustness against disturbances. These properties are strongly related to the cut-off frequencies of the applied filters within the teleoperator control structure. In general, these filters are low-pass filters and may be applied directly at the feedback signals (e.g. the velocity measurement and also the force observer [11]). It can be noted that the high cut-off frequency improves teleoperator performance and consequently the teleoperator transparency. Furthermore, the cut-off frequency is strongly related to the control rate; namely, high control rate allows setting high cut-off frequencies. Thus, high control rate is necessary for high performance bilateral teleoperation. Kubus et al. already addressed the necessity of high control rate [12].

The FPGAs are nowadays widely used among the motion control applications, since it allows high computational power and parallel data processing [13]. It may be used for control applications with very short control and sampling periods [14]. O'Malley and Sevcik presented the comparison of the FPGA platform and commercial system; whereby, the FPGA platform provides up to 400 times greater sampling rates [15]. Moreover, the FPGA provides accurate sampling periods that is usually easy to determine in comparison to the conventional processor-based implementation. Thus, the FPGA is an appropriate solution for bilateral control algorithm implementation in order to

achieve short and accurate sampling periods. Some authors have already adopted FPGA within the bilateral teleoperation research. Tanaka et al. presented multirate bilateral teleoperation system by FGPA [16]. Iishi et al. presented the improvement of performances in bilateral teleoperation by using FPGA [17].

This paper presents a study of the FPGA implementation of the SMC-based bilateral control algorithm [10] as well as the data acquisition algorithms aiming to provide haptic teleoperation. The control law is derived using the chattering-free SMC design approach in the virtual modal space. The presented design methodology allows optimization of the FPGA hardware resources and the execution time of the control algorithm. Furthermore, the design time may be significantly reduced. By the presented design methodology it is possible to achieve short control periods and consequently wide control bandwidth and thus high-performance bilateral teleoperation. The implementation was validated by the master-slave experimental device. As shown, the high-performance bilateral teleoperation was achieved.

The paper structure is as follows. Section 2 describes the bilateral teleoperation problem and its decomposition into virtual modal space. SMC-based control algorithm is also summarized. Section 3 briefly describes the data acquisition algorithms. Section 4 describes the proposed FPGA design methodology. Section 5 shows experimental results. Section 6 concludes the paper.

2 BILATERAL TELEOPERATOR CONTROL

2.1 The system model in the virtual modes

The dynamics of the bilateral teleoperation, as it is depicted by Figure 1, can be described by a simplified model of two robotic mechanisms. Thus, the linearized and decoupled master-slave device dynamics in Cartesian coordinates is given by

$$m_m \ddot{x}_m = f_m + f_h \quad (1)$$

$$m_s \ddot{x}_s = f_s - f_e \quad (2)$$

where m_m , m_s , \ddot{x}_m , \ddot{x}_s , f_m , and f_s are the masses, the accelerations, and the control forces of the master and slave

devices, respectively. f_h is the operator action force and f_e is the environment reaction force.

The design of the bilateral control for transparently optimized architecture can be a difficult task. In order to enhance such a design, it is possible to transform the teleoperator dynamics (1) and (2) into the virtual modal space. The modal transformation is applied by second order Hadamard matrix \mathbf{T} . It decouples master-slave dynamics into two independent virtual coordinates that are associated with the position error and the force error, respectively. Thus, the physical position and force coordinates are transformed into the virtual position and force coordinates as

$$\mathbf{x}_v = \mathbf{T}\mathbf{x} = \begin{bmatrix} 1 & 1 \\ 1 & -1 \end{bmatrix} \begin{bmatrix} x_m \\ x_s \end{bmatrix} = \begin{bmatrix} x_m + x_s \\ x_m - x_s \end{bmatrix} \quad (3)$$

$$\mathbf{f}_v^{ext} = \mathbf{T}\mathbf{f}^{ext} \begin{bmatrix} 1 & 1 \\ 1 & -1 \end{bmatrix} \begin{bmatrix} f_h \\ -f_e \end{bmatrix} = \begin{bmatrix} f_h - f_e \\ f_h + f_e \end{bmatrix} \quad (4)$$

where $\mathbf{x} = [x_m, x_s]^T$, $\mathbf{x}_v = [x_c, x_d]^T$, $\mathbf{f}^{ext} = [f_h, -f_e]^T$, and $\mathbf{f}_v^{ext} = [f_c, f_d]^T$ denote the position vectors and the external force vectors in the physical actuator space and in the virtual modal space, respectively. Indexes $(\cdot)_c$, and $(\cdot)_d$ depicts the common mode, and the differential mode, respectively. It can be noted, that the common mode applies force servoing, while the differential mode applies position tracking. They can be regulated independently in the virtual modal space of the bilateral teleoperation system (1)-(2). Conversely, the inverse modal transformation is applied by $\mathbf{T}^{-1} = \frac{1}{2}\mathbf{T}$. Hence, the teleoperator dynamics can now be expressed in the virtual modes by

$$\mathbf{M}_v \ddot{\mathbf{x}}_v = \mathbf{f}_v + \mathbf{f}_v^{ext} \quad (5)$$

where $\mathbf{M}_v = \mathbf{T}\mathbf{M}\mathbf{T}^{-1}$, and $\mathbf{f}_v = \mathbf{T}\mathbf{f}$ is the mass matrix and the control force in the virtual modal space, respectively. $\mathbf{M} = \text{diag}(m_m, m_s)$, and $\mathbf{f} = [f_m, f_s]^T$ are the mass matrix and control force vector in the physical actuator space, respectively.

2.2 The control objective

Impedance control offers the unified approach for position control as well as force control [18]. To assign the prescribed dynamics of the robot behavior in constraint motion, the impedance control can be utilized to assure stable contact. Thus it may be applied to improve stability while contacting the stiff environment.

The desired second order impedance for the teleoperator system described in the virtual modal coordinates is given by

$$\mathbf{M}_v^d \ddot{\mathbf{x}}_v + \mathbf{B}_v^d \dot{\mathbf{x}}_v + \mathbf{K}_v^d \mathbf{x}_v = \mathbf{f}_v^{ext} \quad (6)$$

where \mathbf{M}_v^d , \mathbf{B}_v^d , and \mathbf{K}_v^d depict the desired mass matrix, the desired damping matrix, and the desired stiffness matrix, respectively. In the paper, the desired impedance parameters are chosen such that $\mathbf{B}_v^d = \mathbf{M}_v^d \mathbf{K}_v$ and $\mathbf{K}_v^d = \mathbf{M}_v^d \mathbf{K}_p$, where \mathbf{K}_v and \mathbf{K}_p are matrices of velocity and position feedback gains in the virtual modes. The matrices are defined as $\mathbf{M}_v^d = \text{diag}(M_c, M_d)$, $\mathbf{K}_v = \text{diag}(0, k_v)$, and $\mathbf{K}_p = \text{diag}(0, k_p)$. M_c and M_d denotes virtual mass in common mode and differential mode, respectively. Then the bilateral operation system dynamics can be expressed in the virtual modes as

$$M_c \ddot{x}_c = f_c \quad (7)$$

$$\ddot{x}_d + k_v \dot{x}_d + k_p x_d = 0 \quad (8)$$

where $f_c = f_h - f_e$. By assumption the virtual masses are chosen such that $0 < M_c < \infty$ and $M_d \rightarrow \infty$.

2.3 The control law

The SMC can be used to design a system that guarantees robustness to system perturbation and external disturbances. This section briefly summarizes the control law derivation, whereas the detailed description of the control law derivation is presented in [10].

The SMC design is applied by the definition of two switching functions σ_c and σ_d which are formed on the basis of the desired modal dynamics (7) and (8)

$$\sigma_c = \ddot{x}_c - f_c/M_c \quad (9)$$

$$\sigma_d = \ddot{x}_d + k_v \dot{x}_d + k_p x_d \quad (10)$$

where index $(\cdot)_c$, and $(\cdot)_d$ refers to the common virtual mode and the differential virtual mode, respectively. If one defines $\boldsymbol{\sigma} = [\sigma_c, \sigma_d]^T$, then switching functions can be written in compact form as

$$\boldsymbol{\sigma} = \ddot{\mathbf{x}}_v + \mathbf{K}_v \dot{\mathbf{x}}_v + \mathbf{K}_p \mathbf{x}_v - \mathbf{M}_v^d \mathbf{f}_v^{ext} \quad (11)$$

Following the SMC design approach, the control law is derived using the requirement $\dot{\boldsymbol{\sigma}} = -D\boldsymbol{\sigma}$. The SMC theory provides the system robustness by a discontinuous control. However, such switching control may be unacceptable for systems with a continuous control input since it can cause an undesired chattering. Therefore, it is necessary to derive chattering-free control. The control law is governed by

$$\mathbf{u} = \mathbf{u}_{eq} - D \int \boldsymbol{\sigma} dt \quad (12)$$

The control signal $\mathbf{u} = [u_c, u_d]^T$ is composed of two components. The first component is the equivalent control $\mathbf{u}_{eq} = [u_{eq,c}, u_{eq,d}]^T$, that is the control signal which is required for the system motion on the sliding

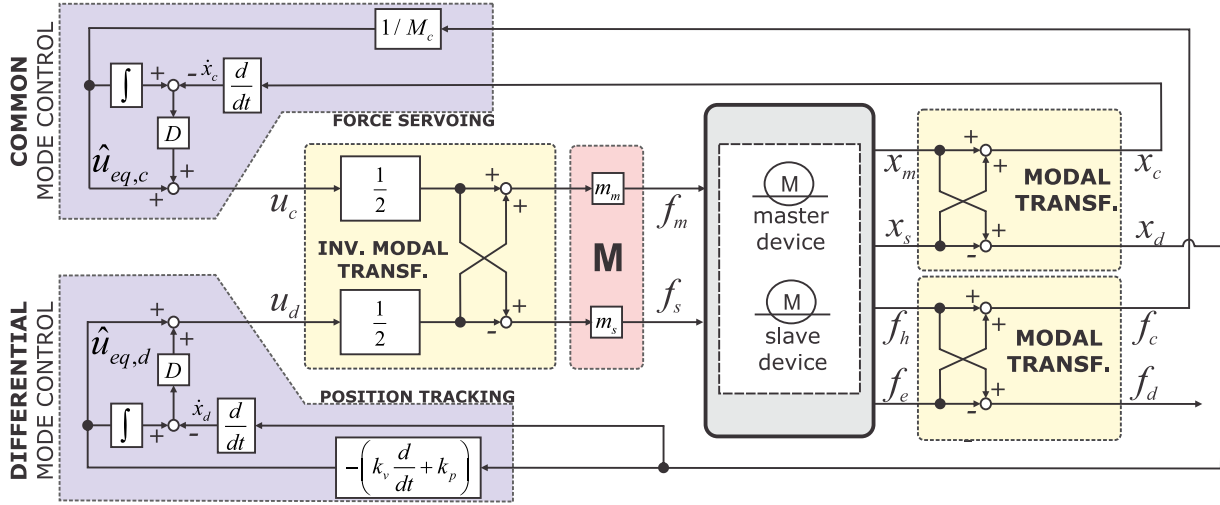


Fig. 2. SMC algorithm for bilateral teleoperation block scheme.

manifold. The equivalent control is calculated by $\mathbf{u}_{eq} = \mathbf{u}^{dist} - (\mathbf{K}_v \dot{\mathbf{x}}_v + \mathbf{K}_p \mathbf{x}_v - \mathbf{M}_v^{d-1} \mathbf{f}_v^{ext})$. The disturbance \mathbf{u}^{dist} is considered to be a non-measurable signal, therefore it is dropped from (12) and \mathbf{u}_{eq} is replaced by $\hat{\mathbf{u}}_{eq}$ that denotes the estimated equivalent control. The second component denotes the system convergence to the sliding manifold. The convergence rate and the disturbance rejection are depended on the chosen value of the robustness parameter D ; higher value provides better robustness of the system. Finally, the control law is expressed such that the acceleration signal is eliminated from the control implementation by using the equality $\int \sigma dt = \dot{\mathbf{x}}_v - \int \hat{\mathbf{u}}_{eq} dt$. It yields

$$\mathbf{u} = \hat{\mathbf{u}}_{eq} + D \left(\int_0^t \hat{\mathbf{u}}_{eq} dt - \dot{\mathbf{x}}_v \right) \quad (13)$$

where $\mathbf{u} = [u_c, u_d]^T$ and $\mathbf{u}_{eq} = [\hat{u}_{eq,c}, \hat{u}_{eq,d}]^T$. The virtual control law of the common and differential modes can be expressed also in the component form

$$u_c = \hat{u}_{eq,c} + D \left(\int \hat{u}_{eq,c} dt - \dot{x}_c \right) \quad (14)$$

$$u_d = \hat{u}_{eq,d} + D \left(\int \hat{u}_{eq,d} dt - \dot{x}_d \right) \quad (15)$$

where $\hat{u}_{eq,c} = f_c/M_c$ and $\hat{u}_{eq,d} = -(k_v \dot{x}_d + k_p x_d)$. Finally, the physical control input vector \mathbf{f} in the master-slave actuator space is governed by

$$\mathbf{f} = \mathbf{M}\mathbf{T}^{-1}\mathbf{u} \quad (16)$$

The SMC-based robust bilateral control scheme is depicted by Figure 2.

The FPGA implementation of the mathematical operations can be optimized such that the number of performed

operations is reduced. The calculation of the physical teleoperator control input (16) can be optimized such that

$$f_m = k_{mc}u_c + k_{md}u_d \quad (17)$$

$$f_s = k_{sc}u_c - k_{sd}u_d \quad (18)$$

where $k_{mc} = m_m/2$, $k_{md} = m_m/2$, $k_{sc} = m_s/2$, and $k_{sd} = m_s/2$ are control gains that can be calculated offline, respectively. The described approach also applies to calculations of x_c , x_d , and $1/M_c$. Such implementation can significantly reduce the number of arithmetical operations and thus the hardware resource consumption is reduced.

3 POSITION, VELOCITY, AND EXTERNAL FORCE CALCULATION ALGORITHMS

3.1 The position measurement

In motion control applications, digital sensors are often used for position measurements, i.e. incremental encoders [16] and digital Hall sensors. Such sensors often suffer from low resolution that is significantly emphasized in low-cost equipment. In order to overcome the problem of low resolution, analog Hall sensors have recently appeared as an advanced solution that benefits low-cost design and yet can provide high resolution measurement. Furthermore, analog Hall sensors may be also integrated within the electrical motor housing. Such a design may significantly contribute within applications where use of external sensors is cumbersome (i.e. MIS).

A linear brushless DC motors (BLDC), used in our research, consists of a moving shaft with the permanent magnets aligned in a pole pairs distributed by the magnetic

pitch. The Hall sensors are integrated within the motor housing to measure the magnetic fields produced by the permanent magnets. The sensors outputs three signals, u_1 , u_2 , and u_3 that are used for shaft position calculation. The calculation applies Clark transformation to two phases u_a and u_b ,

$$\begin{aligned} u_a &= \frac{2}{3}(u_1 - \frac{1}{2}u_2 - \frac{1}{2}u_3) \\ u_b &= \frac{2}{3}(\frac{\sqrt{3}}{2}u_2 - \frac{\sqrt{3}}{2}u_3) \end{aligned} \quad (19)$$

Then the absolute position within a magnetic pitch τm may be calculated by

$$x_\tau = \frac{\tau m}{2\pi} \text{atan2}(u_a, u_b) \quad (20)$$

To calculate the motor shaft position in a full range, the transitions between the magnetic pole pairs k must be counted. Finally, the position x is given by (21).

$$x = x_\tau + k\tau m, \quad k = 0, \pm 1, \pm 2, \dots \quad (21)$$

The position error is strongly dependent on the conversion accuracy of the analog signals. The position error linearly decreases if more accurate A/D converters are applied. The quantization error introduces the position calculation error. Moreover, the analog signals contain noise that may deteriorate the teleoperator sensing bandwidth. In order to minimize the noise that is present in the measured signals, low-pass filters were applied.

3.2 The velocity estimation

This paper presents the velocity estimation algorithm that applies the analog Hall sensors and the $\alpha\beta$ tracker. The latter is a simplified form of the Kalman observer [19]. It acts as a recursive filter and provides positional as well as velocity estimation output. Furthermore, the $\alpha\beta$ tracker can provide satisfactory average characteristics over a wide-range. Position prediction \hat{x}_k^* and the velocity prediction \hat{v}_k^* are described by

$$\hat{x}_k^* = \hat{x}_{k-1} + T_s \hat{v}_{k-1} \quad (22)$$

$$\hat{v}_k^* = \hat{v}_{k-1} \quad (23)$$

where \hat{x}_{k-1} and \hat{v}_{k-1} represents the estimated position and estimated velocity at time instance $k-1$, respectively. T_s is the sampling period. The predicted position and predicted velocity are corrected by

$$\hat{x}_k = \hat{x}_k^* + \alpha(x_k - \hat{x}_k^*) \quad (24)$$

$$\hat{v}_k = \hat{v}_{k-1} + \beta/T_s(x_k - \hat{x}_k^*) \quad (25)$$

where x_k , \hat{x}_k^* , α , and β represent the measured position, predicted position, the position correction gain, and the velocity correction gain, respectively. The $\alpha\beta$ tracker block scheme is depicted by Fig. 3.

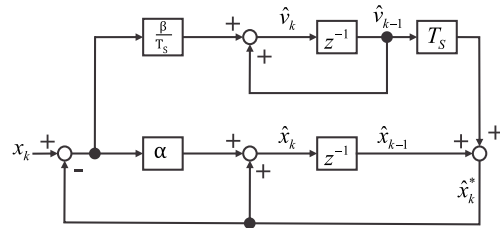


Fig. 3. $\alpha\beta$ tracker block scheme.

The α and β correction gains are defined as the positive constant values and are chosen such that the $\alpha\beta$ tracker addresses the limit Kalman filter. In order to guarantee an asymptotically stable response, α and β are selected within $0 < \alpha < 1$ and $0 < \beta < (2 - \alpha)$, respectively. The values are defined by the system poles and the desired cut-off frequency.

3.3 The external force estimation

The presented control algorithm requires information regarding those external forces that act on the system, i.e. the operator action force as well as the environmental reaction force. Within the applications, where the force sensor is impossible to apply, the reaction and operator forces might be observed by the reaction force observer [20]. Such an observation of the external force signal can also widen the sensing bandwidth.

The external force observer is based on the disturbance observer, which provides an estimation of the disturbance force using a low-pass filter. The estimation algorithm is described by

$$\hat{f}_{ext} = \frac{g}{s+g}(f + gm\dot{x} - \hat{f}_{dist}) - gm\dot{x} \quad (26)$$

where \hat{f}_{ext} , f , \hat{f}_{dist} , \dot{x} , m , and g describe the estimated external force, the control force, the estimation of disturbance force, the measured velocity, the nominal masses of the master or slave devices, and the cut-off frequency of the external force observer, respectively. The disturbance force is always present in the mechatronic systems and is composed of: i) Coulomb friction, ii) viscous friction, iii) interference force, iv) gravity force, and v) perturbation force related parameter variations. Its estimation should be applied with the observer structure in order to estimate the operator action force and the environmental reaction force.

The external force observer block diagram is depicted by Figure 4.

4 FPGA IMPLEMENTATION

The presented design methodology is divided into three stages (Figure 5), whereas the paper deals with the first

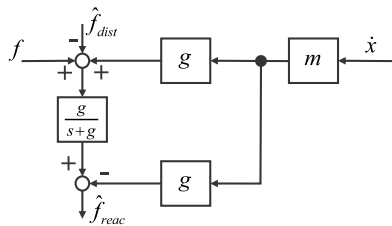


Fig. 4. External force observer block scheme.

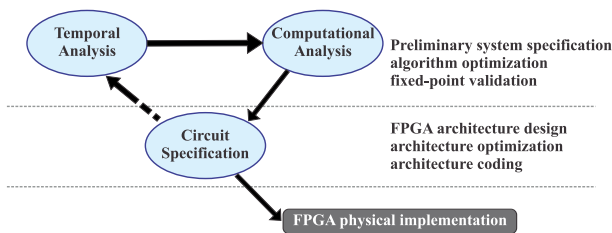


Fig. 5. The FPGA design methodology.

two stages. In the first stage preliminary system specifications are analyzed through the temporal analysis and the computational analysis. Furthermore, basic optimization approaches are utilized to meet the performance requirements. In the second stage, circuit specification is generated either by low-level or high-level programming language. In the last stage, the design is physically implemented on the FPGA.

4.1 Preliminary system specification

4.1.1 Temporal analysis

The tasks can be implemented whether sequential or parallel. They differ in consumed hardware resources and execution time. Depending on the predefined requirements it may be possible to achieve the desired execution time as well as the hardware resources consumption.

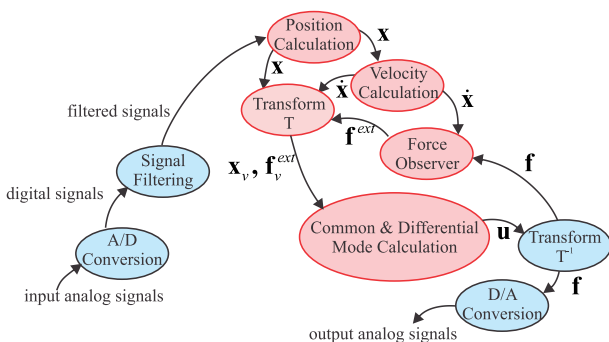


Fig. 6. Data flow diagram.

Figure 6 describes the data flow diagram that defines

the requirements of the tasks execution. It must be noted that the tasks sequence is defined in advance by the control algorithm and cannot be changed. The tasks highlighted with red circles apply for master device as well as for the slave device, respectively. Thus it is possible to physically implement such task only once by the FPGA and execute it sequentially, e.g. to calculate the master position as well as the slave position. Such implementation can significantly reduce the hardware resources consumption; however, on the other hand, the execution time increases. It is possible to achieve higher control rate by shortening execution time to enhance the bilateral teleoperator performance.

Table 1: Tasks execution properties.

Task	Seq. exec.	Cycles	Exec. time
A/D conversion	NO	1	5 μ s
Signal filtering	NO	1	<300 ns
Position calculation	YES	36	450 ns
Velocity calculation	YES	6	75 ns
Modal transformation	YES	4	50 ns
Mode calculation	YES	12	150 ns
Inv. modal transf.	YES	6	75
Ext. force calculation	YES	9	137.5 ns
D/A conversion	NO	1	1 μ s

Table 1 shows the tasks execution properties. Columns, i)Task, ii)Seq. exec., iii)Cycles, and iv)Exec. time, describes the task name, possibility of a sequential implementation, required number of cycles, and execution time respectively. The execution time of the control algorithm can be achieved within a range of 7.2375 μ s and 8.175 μ s. However, the implementation with the minimal execution time of 7.2375 μ s required excessive consumption of the hardware resources to fit the certain FPGA. This can be avoided, either by larger FPGA or increasing the amount of sequential executed tasks. In the paper, the amount of sequential executed tasks was increased such that execution time increased to 8.175 μ s. The bottleneck in achieving higher execution times presents slow A/D and D/A converters. The execution time defines the major limit for the control rate; namely, short execution time allows setting high control rate.

The presented design methodology allows flexibility in terms of implementation as it is described by Figure 7. The tasks highlighted with blue squares depict non-reentrant tasks that may be implemented only parallel, while the tasks highlighted with red squares depicts reentrant tasks that may be implemented also sequentially. As it is shown, when preferring the parallel implementation, execution time is shorter and more hardware resources are required than the sequential implementation, whereas the execu-

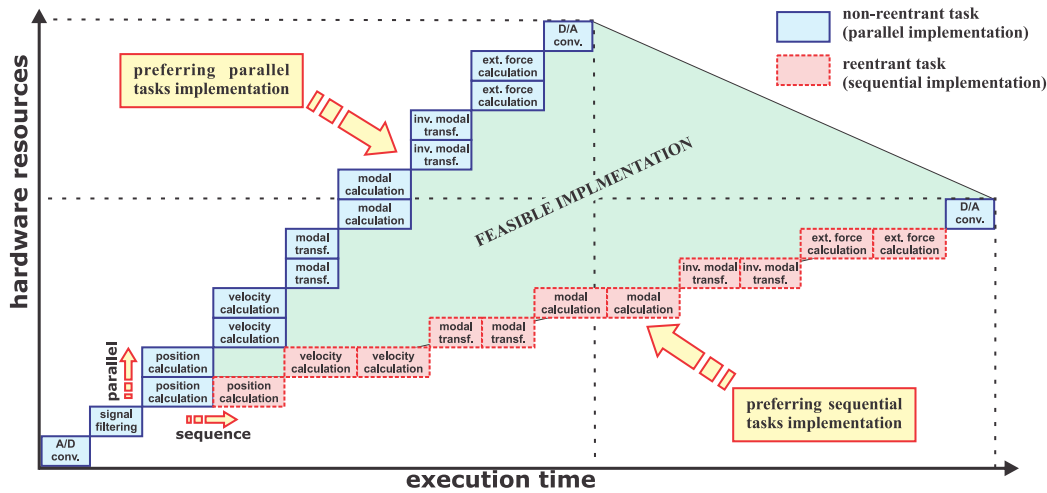


Fig. 7. Comparison of the parallel and sequential tasks implementation.

tion time is shorter. The opposite appears if the sequential implementation is preferred. The implementation can be arbitrary chosen, whereas the feasible implementation is marked by green area. It must be noted, that FPGA size was not considered in the Figure 7 and may also additionally limit the feasible implementation.

4.1.2 Computational analysis

The computational analysis defines the implementation of the mathematical operations and the representation of the values within the calculations. The representation of the values has to be carefully chosen. This can be performed either by using floating-point notation or by using fixed-point notation. The design applies fixed-point data types, since it may provide more optimal hardware resource consumption than the floating-point data type [13]. By the optimal data formats it is possible to significantly reduce the hardware consumption. In this paper, fixed-point notation is described by

$$Q^{L,IL} = \sum_{i=0}^{L-1} b_{i-(L-IL)} \quad (27)$$

where L , IL , and $L-IL$ denote the total number of reserved bits, the number of bits reserved for the integer part, and the number of bits reserved for the fractional part, respectively.

In order to achieve the required data range and precision, the fixed-point notations are chosen by analyzing a signal flow graph. Figure 8 illustrates the signal flow graph for common mode control uc calculation, whereas the fixed-point notation (highlighted with red color) is included to describe each signal. The signal flow graph is designed with the compliance with the following guidelines.

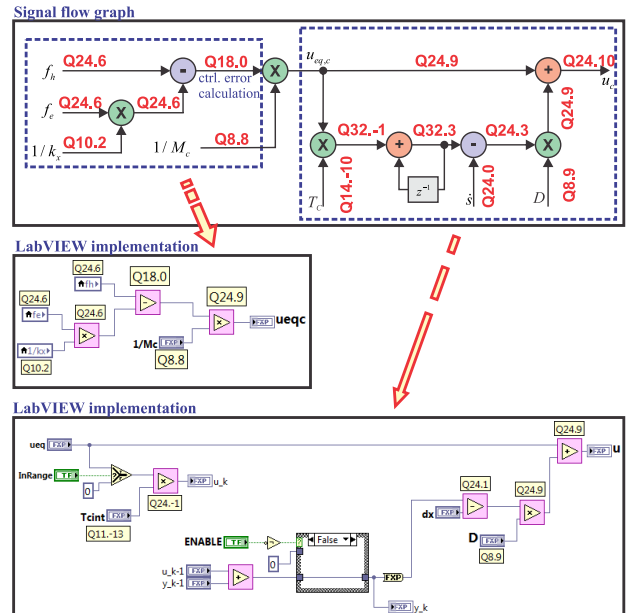


Fig. 8. Signal flow graph section with the corresponding LabVIEW block diagrams.

The input signals data formats as well as the output signals data format were determined by the resolution of the 16-bit A/D and D/A converters. The control parameters were packed into data format of 24 bits max. The data format of the internal signals of the algorithm was determined such that 32-bit data width was not exceeded. In case of applying arithmetic operations such as accumulate (e.g. in integrator or IIR filter such as the $\alpha\beta$ tracker), the internal data format should be wider than the local input-output data format. On the other hand, the data width could be

significantly reduced in case of control error calculation. The expected control error data range may significantly reduce the data width whereas the precision is retained (Figure 8). Similarly, the requirements for an optimal signal representation were thoroughly analyzed through the data flow diagram in order to obtain minimal FPGA resource occupation.

The trigonometric function calculation, such as *atan* is computed by using CORDIC (Coordinate Rotation Digital Computer) [21]. The implementation is based only on simple operations adders/subtractors and shifters. Calculation of *atan2* using CORDIC algorithm is performed by the following equations

$$x_{n+1} = x_n - y_n d_n 2^{-n} \tag{28}$$

$$y_{n+1} = y_n + x_n d_n 2^{-n} \tag{29}$$

$$z_{n+1} = z_n + d_n \text{atan}(2^{-n}) \tag{30}$$

where z is the angle accumulator and $d_n = 1$ if $y_n < 0$ and else $y_n = -1$, $n = 0, 1, \dots, N - 1$, where N is the total number of iterations. As N approaches ∞ , then equations reads

$$x_N = A_N \sqrt{x_0^2 + y_0^2} \tag{31}$$

$$y_N = 0 \tag{32}$$

$$z_N = z_0 + \arctan(y_0/x_0) \tag{33}$$

where

$$A_N = \prod_{k=0}^{N-1} \frac{1}{\cos(\text{atan}(2^{-k}))}. \tag{34}$$

Figure 9 shows LabVIEW property windows of the CORDIC parameters of setting the number of internal iteration and internal word length.

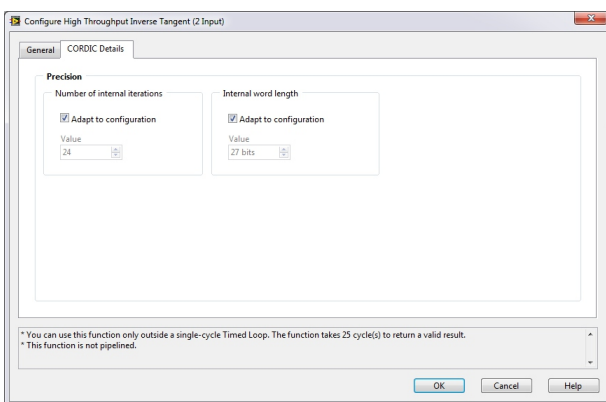


Fig. 9. *atan2* calculation property window.

4.2 Circuit specification

The circuit specification can be performed whether by high-level programming languages, such as LabVIEW [22] and Matlab/Simulink [23], or by low-level programming languages, such as VHDL and Verilog. In the paper, circuit specification was performed by LabVIEW programming environment. Section of the LabVIEW block diagram for common mode calculation is given by Figure 8. Although, the numerical values representation is facilitated by LabVIEW, the computational analysis still remains strongly desired method in order to reduce the hardware resources consumption.

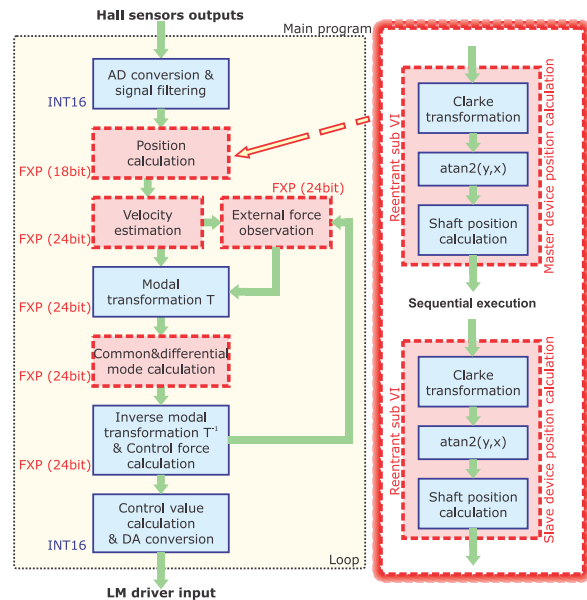


Fig. 10. Concept of tasks implementation.

Based on the preliminary specification, provided by the temporal and computational analysis, the tasks implementation is shown by Figure 10. The tasks highlighted with red squares denote reentrant tasks that are physically implemented only once and are executed repeatedly by different calls from the main program. Such implementation may significantly reduce the hardware resources consumption. It must be noted, that preferring the sequential implementation was necessary in our implementation, since the hardware resources was limited. By larger FPGA it would be possible to increase parallel implementation.

The LabVIEW block diagram (Figure 8) was translated to the VHDL code that describes the logic circuit. Such design allows short design time in comparison to the low-level programming languages, such as VHDL. However, the hardware resources consumption might be higher.

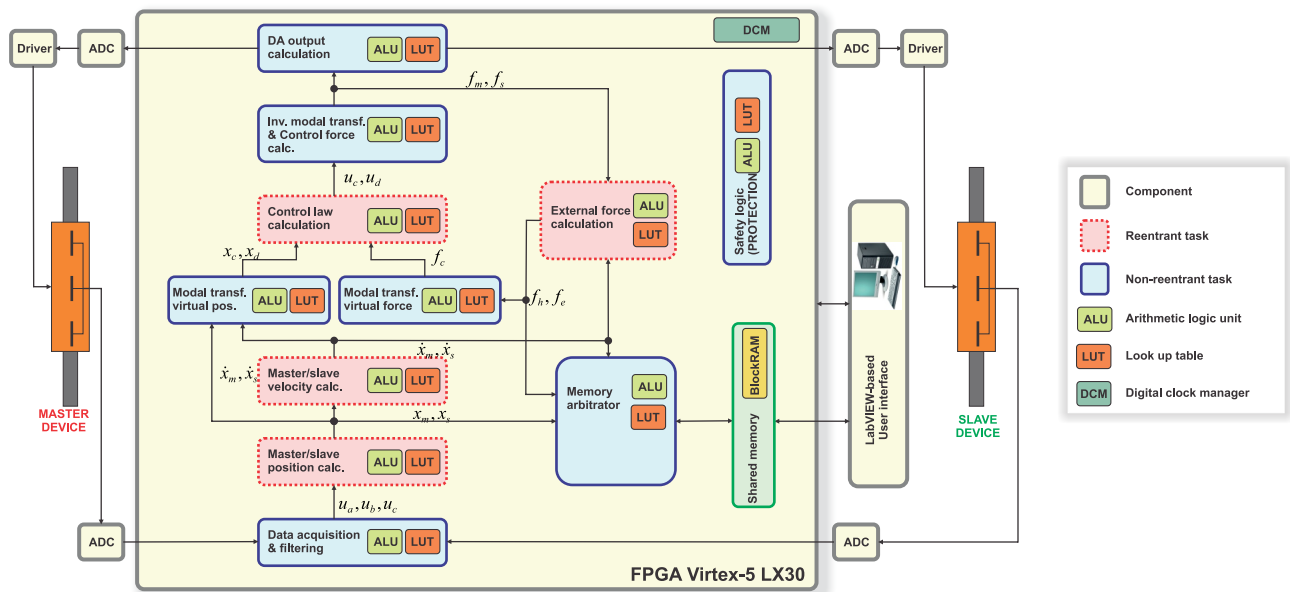


Fig. 11. The implemented FPGA architecture of bilateral teleoperator system.

Table 2: Virtex-5 hardware resources.

Resource	Used	Available	%
SLICES	4792	19200	99.8
FLIP FLOPs	14023	19200	73.0
LUTs	18130	19200	94.4
DSP48e	25	32	78.1
RAM BLOCKs	23	32	71.9

4.3 Hardware resources consumption

The designed FPGA logic circuit consumes many hardware resources (Table 2), though optimization techniques have been applied. Decreasing the precision within the control algorithm calculation would decrease hardware resource consumption; on the other hand, the teleoperator performance would also be deteriorated. The sequential tasks implementation reduces the hardware resource consumption and increases execution time.

The proposed design methodology provides the flexibility in terms of the execution time and available hardware resources, e.g. implementation of the parallel execution of the tasks can be increased when short execution time is required.

Figure 11 describes the overview of bilateral teleoperator configuration, where the FPGA implementation is focused. It can be noted, that tasks are depicted by red and blue squares. Each task is implemented once; whereas the tasks highlighted with red squares are reentrant and executes in a sequence for master device and for slave device,

respectively. Such implementation might significantly reduce the hardware resources; however, on the other hand the execution time increases.

5 EXPERIMENTS

5.1 Experimental setup

The master-slave experimental system is shown by Figure 12. It consists of two linear motors Faulhaber Quick-shaft LM1247-080-01, such that one is the master device and the other is the slave device. The linear motors have integrated analog Hall sensors that are used for the shaft position calculation; hence, no external position sensor was applied. The velocity is estimated using the $\alpha\beta$ tracker. The operator action force as well as the environment reaction force are estimated using the external force observer. The control algorithm outputs reference force that is applied to the motor controller Faulhaber MCLM3006S. The system parameters are depicted by Table 3. The core of the control system was the control board NI PXI-7841R with FPGA Virtex-5 [24].

5.2 Experiments

The control algorithm as well as the data acquisition algorithms implementation was validated by the master-slave experimental system. The following experiments were conducted: free motion, the soft object contact, and the hard object contact. The manipulator and the bilateral control parameters are depicted by Table 3 and Table 4, respectively.

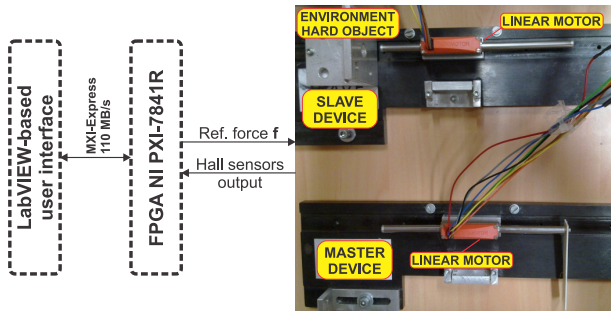


Fig. 12. Experimental test-bed.

Table 3: Manipulator parameters.

Manipulator parameter		Value
Maximum force f_{max}	N	3.6
Magnetic pitch τ_m	mm	18
Hall sensors peak-peak voltage V_{pp}	V	3
ADC voltage resolution Q	V	$20/2^{16}$
Master device mass m_m	g	35
Slave device mass m_s	g	35

The experimental results are displayed by Figures 13-14. Figure 13 shows the results for the unconstrained bilateral teleoperation. Figure 14 shows the constrained motion that is furthermore divided into two subfigures, soft object contact (Figure 14a) and hard object contact (Figure 14b). Each result is depicted by two separate plots; whereby, the first displays the position tracking performance, and the second displays the forces serving performance. The master device position x_m and the operator force f_h are depicted with a solid red line. The slave device position x_s and the environment force f_e are depicted with a dashed green line.

During the unconstrained motion (Figure 13), excellent position tracking as well as excellent force servoing was observed. Although, the slave device is not in contact with the environment, the estimated operators force f_h as well as environment force f_e is not 0N. The reasons for such estimation are the disturbances, such as the mass of the shaft, noisy analog signals from the Hall sensors, and the discretization by the A/D converters. The system noise is reflected in the velocity and furthermore in the external forces.

During the constrained motion (Figure 14), the slave device is touching foam (Figure 14a) and aluminum (Figure 14b). The position tracking deteriorates in conjunction with stiffness; meaning, increasing stiffness is deteriorating position tracking. On the other hand, excellent force servoing was achieved for both situations, for soft object contact as well as for hard object contact.

Table 4: Control parameters.

Control parameters		Value
Position corection gain α		0.1105
Velocity corection gain β		0.0032
$\alpha\beta$ tracker cut-off frequency ω_0	rad/s	300
Force observer cut-off frequency g	rad/s	300
Robust gain D	1/s	300
Position gain k_p	1/s	14400
Velocity gain k_v	1/s ²	240
Virtual mass M_c	g	35
Sampling and control period T_s	μ s	20

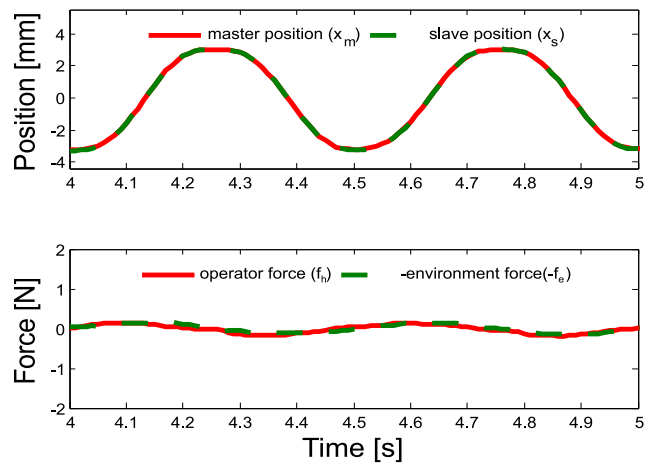


Fig. 13. Free (unconstrained) motion.

It should be mentioned, that the hard object contact in the remote environment is rather difficult to present to the human operator with high-haptic fidelity. In order to achieve high-performance bilateral teleoperation, the control parameters must be chosen with compliance of the following guidelines. Better tracking performance can be achieved by higher control parameters D , k_p , k_v , and lower virtual mass M_c . Higher robust gain D increases the robustness to the system perturbations. Larger position gain k_p increases the control bandwidth and properly tuned velocity gain k_v provides desired damping. In order to determine the values for k_v and k_p the design procedure considers the prescribed dynamics of the simple 2nd order system, which poles are determined by characteristic polynomial of the closed-loop system (35).

$$s^2 + k_v s + k_p \tag{35}$$

This initial phase provides only the coarse parameters tuning for the desired cut-off frequency and damping of the closed-loop, while the fine tuning for enhanced position tracking performance is done by trial-and-error method.

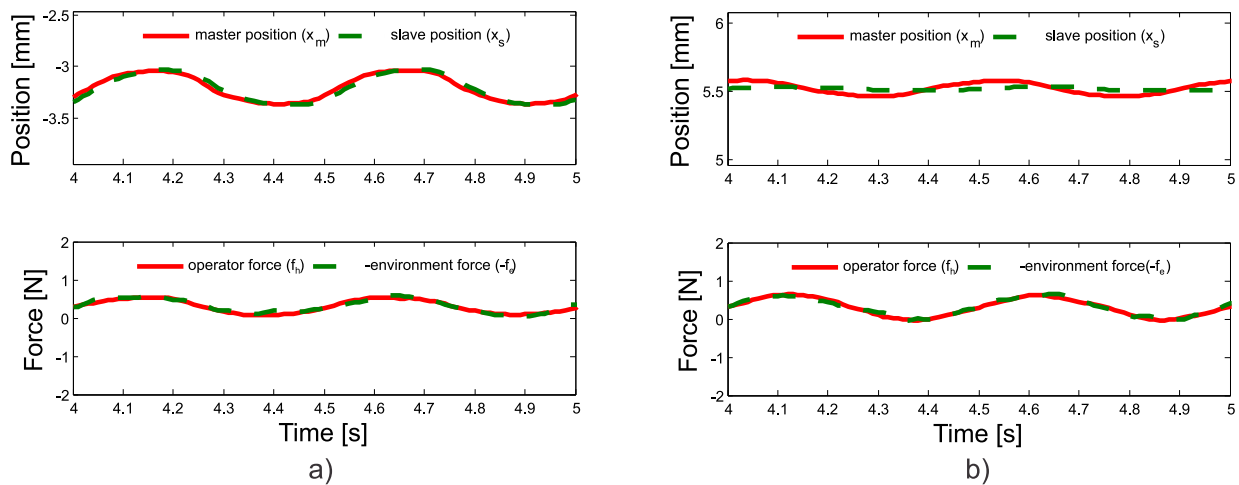


Fig. 14. Contact (constrained) motion: soft object contact (a) and hard object contact (b).

Lower virtual mass M_c improves the force tracking. Hace et al. investigated the impact of the control parameters on the system performance in [25].

In the control parameters design major limitation is the presence of the system noise. The latter reflects in the noisy velocity and the estimated external force signals. The velocity noise appears due to the noisy analog signals from the Hall sensors, discretization by AD converters, and could be improved by optimal filtering. Higher control parameters provide enhanced performance that could be achieved if high-quality measured signals with zero noise and phase lag were obtained. However, the high signal/noise ratio of the measured signals and high phase lag can deteriorate the teleoperator performance; therefore signal quality is important in the control design to achieve high performance haptic fidelity.

6 CONCLUSION

This paper addresses the problem of haptic teleoperation. The presented study of the FPGA implementation of the sliding mode control algorithms for bilateral teleoperation leads toward high haptic fidelity. The control law was derived using the modal decomposition and the chattering-free SMC design approach, respectively.

The presented design methodology allows FPGA hardware resources consumption and the execution time of the control algorithm optimization. Furthermore, it allows short design time, although the flexible requirements that appears during experimental research. Due to the FPGAs well-known performance, short and accurate sampling and control periods were achieved. The periods can be significantly shorter that could be achieved by the conventional processor-based implementation [15]. Consequently, larger feedback gains and wider bilateral control bandwidth were possible to tune.

The implementation was validated by the master-slave experimental system. As it was successfully shown, excellent tracking performance was achieved for unconstrained as well as for constrained motion. Major limitation in setting the control rate is defined by slow A/D ($5 \mu\text{s}$) and D/A ($1 \mu\text{s}$) converters. This furthermore affects the tuning of feedback control gains. In a practical control application, the values of control gains are often limited by the implemented control rate. The other limitation in control parameters tuning presents the system noise. Nevertheless, the achieved control rate was significantly higher compared to commercially systems [12]. Such implementation can enhance the tracking performance of the bilateral controller and leads towards the high haptic fidelity.

ACKNOWLEDGMENT

Operation part financed by the European Union, European Social Found.

REFERENCES

- [1] P. Puangmali, H. Liu, L. D. Seneviratne, P. Dasgupta, and K. Althoefer, "Miniature 3-Axis Distal Force Sensor for Minimally Invasive Surgical Palpation," *IEEE/ASME Trans. Mechatronics*, vol. 17, no. 4, pp. 646-656, Aug. 2012.
- [2] M. T. Perri, A. L. Trejos, M. D. Naish, R. V. Patel, and R. A. Malthaner, "Initial Evaluation of a Tactile/Kinesthetic Force Feedback System for Minimally Invasive Tumor Localization," *IEEE/ASME Trans. on Mechatronics*, vol. 15 no. 6, pp. 925-931, Dec. 2010.
- [3] P. F. Hokayem, and M. W. Spong, "Bilateral teleoperation: An historical survey," *Automatica*, vol. 42, pp. 2035-2057, Dec. 2006.

- [4] Y. Yokokohji, and T. Yoshikawa, "Bilateral Control of Master-Slave Manipulations for Ideal Kinesthetic Coupling – Formulation and Experiment," *IEEE Trans. on Robotics and Automation*, vol.10, no.5, pp.605–620, Oct. 1994.
- [5] K. Vlachos, and E. Papadopoulos, "Transparency Maximizing Methodology for Haptic Devices," *IEEE/ASME Trans. on Mechatronics*, vol. 11 no. 3, pp. 249-255, June 2006
- [6] H. Tanaka, K. Ohnishi, H. Nishi, T. Kawai, Y. Morikawa, S. Ozawa, and T. Furukawa, "Implementation of Bilateral Control System Based on Acceleration Control using FPGA for Multi-DOF Haptic Endoscopic Surgery Robot," *IEEE Trans. Industrial Electronic*, vol. 56 no. 3, pp. 618-627, March 2009.
- [7] V. I. Utkin, "Sliding Modes in Control and Optimization", Springer-Verlag, Berlin, 1992.
- [8] S. Khan, A. Sabanovic, and A. O. Nergiz, "Scaled Bilateral Teleoperation Using Discrete-Time Sliding-Mode Controller," *IEEE Trans. Industrial Electronics*, vol. 56 no. 9, pp. 3609-3618, Sept. 2009.
- [9] K. Ohnishi, S. Katsura, and T. Shimono, "Motion Control for Real-world Haptics," *IEEE Industrial Electronics Magazine*, vol. 4, no. 2, pp. 16-19, June 2010.
- [10] A. Hace, M. Franc, and K. Jezernik, "Sliding Mode Control for Scaled Bilateral Teleoperation," in *37th Proc. IEEE Conf. IECON 2011*, pp. 3430-3435, 2011.
- [11] S. Katsura, Y. Matsumoto, and K. Ohnishi, "Realization of Law of Action and Reaction by Multilateral Control," *IEEE Trans. Industrial Electronics*, vol. 52, no. 5, pp. 1196-1205, Oct. 2005.
- [12] D. Kubus, I. Weidauer, and F.M. Wahl, "1kHz is not enough — How to achieve higher update rates with a bilateral teleoperation system based on commercial hardware", in *Proc. IEEE/RSJ Int. Conf. on Intelligent Robots and Systems (IROS 2009)*, pp. 5107-5114, 2009.
- [13] E. Monmasson, and M. N. Cirstea, "FPGA Design Methodology for Industrial Control Systems—A Review," *IEEE Trans. on Industrial Electronics*, vol. 54, no. 4, pp. 1824-1842, Aug. 2007.
- [14] E. Monmasson, L. Idkhajine, M. N. Cirstea, I. Bahri, A. Tisan, and M. W. Naouar, "FPGAs in Industrial Control Applications," *IEEE Trans. Industrial Informatics*, vol. 7, no. 2, pp 224-243, May 2011.
- [15] M.K. O'Malley, and K.S. Sevcik, "Improved Haptic Fidelity Via Reduced Sampling Period With an FPGA-Based Real-Time Hardware Platform", *J. Comput. Inf. Sci. Eng.*, vol. 9, no. 1, pp. 1-7, March 2009.
- [16] H. Tanaka, K. Ohnishi, and H. Nishi, "Implementation of Multirate Acceleration Control Based Bilateral Control System Including Mode Transformation on FPGA," in *Proc. IEEE Conf. IECON*, Orlando, 2008, pp. 2465-2470.
- [17] E. Iishi, H. Nishi, and K. Ohnishi, "Improvement of Performances in Bilateral Teleoperation by Using FPGA," *IEEE Trans. Industrial Electronics*, vol. 54, no. 4, pp. 1876-1884, Aug. 2007.
- [18] N.Hogan, "Impedance Control: An Approach to Manipulation, Part I, II, III," *Journal of Dynamic Systems, Measurement, and Control*, vol.107, no. 1, pp.1-23, March 1985.
- [19] E. P. Cunningham, "Digital Filtering: An Introduction," *Houghton Mifflin Company*, Boston, 1992.
- [20] S. Katsura, Y. Matsumoto, and K. Ohnishi, "Modeling of Force Sensing and Validation of Disturbance Observer for Force Control," *IEEE Trans. Industrial Electronics*, vol. 54, no. 1, pp. 530-538, Feb. 2007.
- [21] L. Vachhani, K. Sridharan, and P. K. Meher, "Efficient FPGA realization of CORDIC with application to robotic exploration," *IEEE Trans. Industrial Electronics*, vol. 56, no. 12, p. 4915, Dec. 2009
- [22] T. O. Kowalska, and M. Kaminski, "FPGA Implementation of the Multilayer Neural Network for the Speed Estimation of the Two-Mass Drive System," *IEEE Trans. Industrial Informatics*, vol. 7, no. 3, pp. 436-445, Aug. 2011.
- [23] B. Alecsa, M. Cirstea, and A. Onea, "Simulink Modelink and Design of an Efficient Hardware-constrained FPGA-based PMSM Speed Controller," *IEEE Trans. Industrial Informatics*, vol. PP, no. 99.
- [24] Virtex-5 Family Overview, Product Specification, DS100 (v5.0), Feb. 6, 2009
- [25] M. Franc, and A. Hace, "Robust Haptic Teleoperation by FPGA," Accepted for presentation at SYROCO 2012.



Marko Franc received the B.S. in electrical engineering from the University of Maribor, Maribor, Slovenia, in 2009. In 2009 he joined Institute of Robotics, Faculty of Electrical and Computer Science, University of Maribor, where he is a PhD student. His research interests include motion control, haptics, and mechatronics.



Aleš Hace received the B.S., M.S., and Ph.D. degrees in electrical engineering from the University of Maribor, Maribor, Slovenia, in 1994, 1998, and 2001, respectively. In 1994, he joined the Institute of Robotics, Faculty of Electrical and Computer Science, University of Maribor, where he has been holding the position of an Assistant Professor for Automation and Robotics since 2006. In 2010 he has been elected Associate Professor. In 1999, he was a Visiting Research Fellow at Loughborough University, Leicestershire, U.K. The main areas of his research are related to the areas of mechatronics, robotics, servodrives, and sliding-mode control. Dr. Hace was the recipient of the Bedjanic Slovenian National Research Award in 1998. He is IEEE Member of its Industrial Electronics Society, and member of national Automatic Control Society of Slovenia.

AUTHORS' ADDRESSES

Marko Franc
ISOMAT d.o.o.
Mežica, Slovenia
email: marko.franc@uni-mb.si

Prof. Aleš Hace, Ph.D.
Institute of Robotics
Faculty of Electrical and Computer Science
University of Maribor
Maribor, Slovenia
email: ales.hace@uni-mb.si

Received: 2012-06-22

Accepted: 2012-10-15